Quantum interference and light polarization effects in unresolvable atomic lines: Application to a precise measurement of the ^{6,7}Li D_2 lines

Roger C. Brown,[1,2] Saijun Wu,[1,2,*] J. V. Porto,[1,2] Craig J. Sansonetti,[1] C. E. Simien,[1,2,†] Samuel M. Brewer,[1,2,‡]
Joseph N. Tan,[1] and J. D. Gillaspy[1]

[1]*National Institute of Standards and Technology, Gaithersburg, Maryland 20899, USA*
[2]*University of Maryland, College Park, Maryland 20742, USA*
(Received 2 December 2012; published 7 March 2013)

We characterize the effect of quantum interference on the line shapes and measured line positions in atomic spectra. These effects, which occur when the excited-state splittings are of order of the natural line widths, represent an overlooked but significant systematic effect. We show that excited-state interference gives rise to non-Lorentzian line shapes that depend on excitation polarization, and we present expressions for the corrected line shapes. We present spectra of ^{6,7}Li D lines taken at multiple excitation laser polarizations and show that failure to account for interference changes the inferred line strengths and shifts the line centers by as much as 1 MHz. Using the correct line shape, we determine absolute optical transition frequencies with an uncertainty of $\leqslant 25$ kHz and provide an improved determination of the difference in mean-square nuclear charge radii between ^{6}Li and ^{7}Li. This analysis should be important for a number of high-resolution spectral measurements that include partially resolvable atomic lines.

I. INTRODUCTION

The measurement of accurate atomic transition frequencies plays an important role in fundamental physics from atomic clocks to the determination of nuclear charge radii. Determining accurate frequencies requires a sufficient understanding of the transition line shape. In particular, the Lorentzian line shape is of fundamental importance in the analysis of resonant phenomena in many areas of physics [1]. When two or more resonances are separated by the order of a natural line width, unresolvable in a fundamental sense not limited by instrumentation, there arises the possibility of interference. The resulting line shape is, in general, no longer a simple sum of Lorentzians, even in the low-intensity limit. Although this effect has been known in different contexts for many years [2–5], it has typically been ignored in the interpretation of Doppler-free spectra. In our previous work [6], we demonstrated that quantum interference has an observable effect on atomic spectra, which can limit accuracy if not properly accounted for. In Sec. II of this article, we derive a more general set of lineshapes and estimate the systematic errors incurred if strictly Lorentzian line shapes are assumed. In Sec. III, we use the more complete line shapes to extract absolute transition frequencies from ^{6,7}Li data, including previously unpublished data, and to quantify errors associated with incomplete line shapes. Finally, in Sec. IV, we use our measurement of the ^{6,7}Li D line isotope shift to extract the relative ^{6,7}Li difference in mean-square nuclear charge radius. The unresolvable hyperfine structure in the D_2 lines of hydrogen [7], lithium [6], potassium [8], francium [9], singly ionized beryllium [10], and magnesium [11] are additional examples where interference-modified Lorentzian line shapes are expected.

II. DIPOLE SCATTERING LINE SHAPE

We begin with a derivation of the corrected line shape, including quantum interference terms, using the Kramers-Heisenberg formula [12], which describes the differential scattering rate of light incident on an atom initially in the state $|i\rangle$ and ending in the state $|f\rangle$. It can be derived from Fermi's golden rule [13]:

$$\frac{dR_{i \to f}}{d\Omega_s} = \frac{2\pi}{\hbar} |M_{fi}|^2 \rho_s, \qquad (1)$$

where $\hbar$ is Planck's constant (h) divided by 2π and ρ_s is the density of scattered photon states into a solid angle $d\Omega_s$ along the scattering direction $\mathbf{k}_s$. The scattering matrix element M_{fi} is calculated to second order in the electric-dipole coupling. The scattering matrix element depends on the frequency, wave vector, and polarization of the incident light ($\omega_{\rm L}$, $\mathbf{k}_{\rm L}$, $\hat{\epsilon}_{\rm L}$) and scattered light (ω_s, $\mathbf{k}_s$, $\hat{\epsilon}_s$). The resulting scattering rate is

$$\frac{dR_{i \to f}}{d\Omega_s} = \frac{\pi E_{\rm L}^2 \omega_s^3}{h^3 c^3 \epsilon_0} \left| \sum_j \frac{(\hat{\epsilon}_s^* \cdot \mathbf{D}_{fj})(\mathbf{D}_{ji} \cdot \hat{\epsilon}_{\rm L})}{\omega_{ji} - \omega_{\rm L} - i\Gamma_j/2} \right|^2, \qquad (2)$$

where c is the speed of light, ϵ_0 is the permittivity of free space, and $E_{\rm L}$ is the amplitude of the electric field of the incident light. The sum is over excited intermediate states $|j\rangle$ with transition frequencies ω_{ji} and atomic dipole matrix elements $\mathbf{D}_{ji} = \langle j|e\mathbf{r}|i\rangle$. Here e is the electron charge and $\mathbf{r}$ is the position operator of the valence electron. The finite lifetime of the excited states $|j\rangle$ are accounted for [12] by including the imaginary part $i\Gamma_j/2$ in the transition frequency ω_{ji} [14]. Here Γ_j is the inverse lifetime (or full width half maximum for an isolated Lorentzian line) of $|j\rangle$. Equation (2), valid in the low-excitation-intensity limit, does not include multiple

scattering effects like optical pumping. Additionally, we make the rotating wave approximation, which is appropriate for near-resonant excitation. While Eq. (2) is a Lorentzian distribution if only one term of the sum is considered, since the sum over intermediate states is *inside* the square, one can see that interference from different excited states $|j\rangle$ is possible.

For a concrete experimental comparison, we restrict our analysis to the case where states $|i\rangle$ and $|f\rangle$ are hyperfine states of a single electronic ground state with electronic angular momentum J, and the intermediate hyperfine states $|j\rangle$ belong to a single excited electronic state with angular momentum J'. The states are labeled by their total angular momentum and z projection of angular momentum $|F_i, m_i\rangle$, $|F_f, m_f\rangle$, and $|F', m'\rangle$.

One can evaluate the atom-field coupling matrix element by repeatedly applying the Wigner-Eckart theorem. The reduced matrix elements can be written in terms of the electronic excited state linewidth Γ and a reference intensity I_0 (see Appendix A). (For a closed transition such as the Li $2s$-$2p$ transitions considered here, $\Gamma = \Gamma_j$.) This gives

$$\frac{dR_{i\to f}}{d\Omega_s} = \frac{3}{8\pi}\frac{I}{I_0}\left(\frac{\Gamma}{2}\right)^3 \left|\sum_{F'm'} \frac{\left(\hat{\epsilon}_s \cdot \mathbf{A}_{F_f m_f}^{F'm'}\right)\left(\mathbf{A}_{F_i m_i}^{F'm'} \cdot \hat{\epsilon}_L\right)}{\Delta_{F_i}^{F'} + i\Gamma/2}\right|^2. \tag{3}$$

Here $\Delta_{F_i}^{F'} = \omega_L - \omega_{F'F_i}$, and $\mathbf{A}_{F_f m_f}^{F'm'}$ are the normalized dipole matrix elements containing all the angular dependence of the atomic dipole. The explicit form for $\mathbf{A}_{F_i m_i}^{F'm'}$ is given in Appendix A.

Since the denominator in Eq. (3) is independent of m', we can sum the numerator over m'. Defining the function

$$C_{i\to f}^{F'}(\hat{\epsilon}_s, \hat{\epsilon}_L) = \sum_{m'}\left(\hat{\epsilon}_s \cdot \mathbf{A}_{F_f m_f}^{F'm'}\right)\left(\mathbf{A}_{F_i m_i}^{F'm'} \cdot \hat{\epsilon}_L\right), \tag{4}$$

we have

$$\frac{dR_{i\to f}}{d\Omega_s} = \frac{3}{8\pi}\frac{I}{I_0}\left(\frac{\Gamma}{2}\right)^3 \left|\sum_{F'} \frac{C_{i\to f}^{F'}(\hat{\epsilon}_s, \hat{\epsilon}_L)}{\Delta_{F_i}^{F'} + i\Gamma/2}\right|^2, \tag{5}$$

where $C_{i\to f}^{F'}(\hat{\epsilon}_s, \hat{\epsilon}_L)$ depends on the initial- and final-state quantum numbers F_i, m_i, F_f, and m_f.

Equation (5) describes the differential scattering rate of light into solid angle $d\Omega_s$ (along $\mathbf{k}_s$) with polarization $\hat{\epsilon}_s$ for atoms starting in state $|F_i, m_i\rangle$ and ending in $|F_f, m_f\rangle$. In a typical spectroscopy experiment, the final scattering state is unresolved, so the scattering rate $R_{F_i m_i \to F_f m_f}$ is summed over final states F_f and m_f. To further simplify the discussion, we assume the detection is polarization insensitive and sum over the two scattered polarizations $\hat{\epsilon}_s \perp \mathbf{k}_s$ for a given detection direction $\mathbf{k}_s$. If, in addition, we assume an unpolarized atomic sample, we must average over all initial m_i. Summing and evaluating the square in Eq. (5) gives rise to sums of Lorentzian components and cross terms:

$$\frac{dR_{F_i}(\hat{\epsilon}_L)}{d\Omega_s} = \frac{1}{4\pi}\frac{I}{I_0}\left(\frac{\Gamma}{2}\right)^3 \left(\sum_{F'} \frac{f(\mathbf{k}_s, \hat{\epsilon}_L, F_i, F')}{\left(\Delta_{F_i}^{F'}\right)^2 + (\Gamma/2)^2}\right.$$

$$\left. + \sum_{F' \neq F''} 2\mathrm{Re}\left[\frac{g(\mathbf{k}_s, \hat{\epsilon}_L, F_i, F', F'')}{\left(\Delta_{F_i}^{F'} + i\Gamma/2\right)\left(\Delta_{F_i}^{F''} - i\Gamma/2\right)}\right]\right), \tag{6}$$

where the line strengths $f(\mathbf{k}_s, \hat{\epsilon}_L, F_i, F')$ and cross-term strengths $g(\mathbf{k}_s, \hat{\epsilon}_L, F_i, F', F'')$ for a particular laser polarization and detected direction are given by

$$f(\mathbf{k}_s, \hat{\epsilon}_L, F_i, F') = \frac{3}{2g_T}\sum_{s, m_i F_f m_f}\left|C_{i\to f}^{F'}(\hat{\epsilon}_s, \hat{\epsilon}_L)\right|^2,$$

$$g(\mathbf{k}_s, \hat{\epsilon}_L, F_i, F', F'')$$
$$= \frac{3}{2g_T}\sum_{s, m_i F_f m_f} C_{i\to f}^{F'}(\hat{\epsilon}_s, \hat{\epsilon}_L)\left[C_{i\to f}^{F''}(\hat{\epsilon}_s, \hat{\epsilon}_L)\right]^*, \tag{7}$$

where $g_T = \sum_i (2F_i + 1)$ is the total number of Zeeman states in the ground electronic state, assumed here to be uniformly thermally populated. When the excited-state hyperfine splitting is not well resolved, $\Delta_{F_i}^{F'} - \Delta_{F_i}^{F''} \equiv \Delta_{F'}^{F''} \approx \Gamma$, then the cross terms are not necessarily negligible, as implicitly assumed in the latter portion of Ref. [15].

A. Angular dependence

Dipole scattering of light follows a dipole radiation pattern [16], which for linearly polarized light depends only on the angle γ between excitation laser polarization ϵ_L and the fluorescence collection direction $\mathbf{k}_s$. The angular dependence of the dipole scattering is proportional to $\cos^2\gamma$ and can always be written as a sum of a spherically symmetric component and a dipole component $[A_{\mathrm{tot}} + BP_2(\cos(\gamma))]/(4\pi)$. Here A_{tot} is the total line strength integrated over all solid angle, $P_2(x) = (3x^2 - 1)/2$ is the second Legendre polynomial (which has zero integral over solid angle), and B characterizes the amplitude of the angular dependence. By construction, f contains all the scattering line strength, the integral over solid angle of the cross terms g, proportional to $P_2(\cos\gamma)$, vanishes. A consequence of this angular dependence is that $f(\mathbf{k}_s, \hat{\epsilon}_L, F_i, F')$ does *not* provide the correct ratio of line strengths of the $F_i \to F'$ transitions for an arbitrary choice of detection direction, γ, since B/A_{tot} is not the same for different F'. As we will show, however, there exist "magic" orientations where f does give line strengths consistent with resolved transitions. More importantly, at these magic conditions the cross terms g vanish, giving rise to purely Lorentzian line shapes.

We parametrize γ in terms of angles relevant to an experimental geometry. The wave vectors $\hat{k}_L$ and $\hat{k}_s$ define a plane which we take to be the $\hat{x}$-$\hat{z}$ plane. Without loss of generality we can take $\hat{k}_L$ along $\hat{x}$, so that $\hat{\epsilon}_L$ lies in the $\hat{y}$-$\hat{z}$ plane, making an angle θ_L with respect to $\hat{z}$, and $\hat{k}_s$ lies in the $\hat{x}$-$\hat{z}$ plane making an angle θ_s with respect to $\hat{z}$ (see Fig. 1). The scattering is then parameterized by the linearly independent angles θ_s and θ_L; $f(\mathbf{k}_s, \hat{\epsilon}_L, F_i, F') = f(\theta_s, \theta_L, F_i, F')$ and similarly for g [17]. The spherical harmonic addition theorem [18] can be used to relate $P_2(\cos\gamma)$ to θ_s and θ_L:

$$P_2(\cos\gamma) = \tfrac{1}{2}(3\cos^2\theta_s \cos^2\theta_L - 1). \tag{8}$$

The general form for f and g is then

$$f(\theta_s, \theta_L, F, F') = A_F^{F'} + \frac{B_F^{F'}}{2}(3\cos^2\theta_s \cos^2\theta_L - 1),$$
$$\tag{9}$$
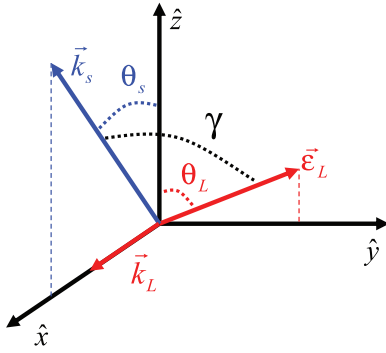$$g(\theta_s, \theta_L, F, F', F'') = \frac{C_F^{F'F''}}{2}(3\cos^2\theta_s \cos^2\theta_L - 1),$$

FIG. 1. (Color online) Coordinate system: The excitation laser propagates along $\hat{x}$ so that the linear polarization direction $\hat{e}_L$ lies in the $\hat{y}$-$\hat{z}$ plane, parameterized by θ_L. The detection direction k_s lies in the $\hat{x}$-$\hat{z}$ plane and is parameterized by θ_s. In our apparatus, light collection is centered along $\hat{z}$ with an angular spread determined by the numerical aperture of the imaging system. The atomic beam is along $\hat{y}$.

where $A_F^{F'}$, $B_F^{F'}$, and $C_F^{F'F''}$ are constants determined by evaluating Eq. (7). When $\cos\theta_s \cos\theta_L = 1/\sqrt{3}$, g vanishes and f correctly gives the line-strength ratios. This can occur for a range of geometries. In particular, when the detection $\mathbf{k}_s$ is orthogonal to the excitation $\mathbf{k}_L$ ($\theta_L = \gamma$, $\theta_s = 0$) as in our apparatus [6], then $\theta_L = \arccos(\frac{1}{\sqrt{3}}) \equiv \theta_M \approx 54.73^\circ$ is the so-called "magic" angle. Similar magic-angle effects occur in quantum beat spectroscopy, which could be viewed as a time-domain analog of the effect considered here, where the excitation pulse width replaces the natural width [19,20]. Explicit expressions for $f(\theta_L, F_i \to F')$ and $g(\theta_L, F_i \to F', F_i \to F'')$ are evaluated for lithium with the collection along the $\hat{z}$ direction in Appendix B.

B. Line-shape impact on extracted frequencies

We now give a qualitative discussion of the effect of the additional interference terms on Doppler-free, or nearly free, spectra. We choose ^{6,7}Li as an example because of its fundamentally unresolvable structure ($\Delta_{F'}^{F''}/\Gamma \approx 1$) and because it allows for direct comparison to experimental data. Figure 2 illustrates two primary effects. First, the maxima of the total line shape are shifted relative to what is predicted by a simple sum of Lorentzian distributions, which can lead to errors in extracting the weighted line center. Second, peaks may vary in intensity and prominence depending on the polarization angle of the laser. For example in Fig. 2, $\theta_L = 0$, the amplitude of the $F = 2 \to F' = 3$ component is reduced with respect to the $F = 2 \to F' = 2$ component.

Line centers are typically determined by fitting a sum of Lorentzian functions to the observed spectral profile. We characterize the effect of cross terms on line centers (both of individual hyperfine components and of centers of gravity of composite features) by taking a Doppler-free line shape given by Eq. (7) with cross terms and fitting to it using only Lorentzian functions (amplitude, center, offset, linewidth). We then compare the centers given by Eq. (7) to the centers extracted from the fit to estimate the effect of the cross terms on measured quantities. From Eq. (9) (with $\theta_L = \gamma$, $\theta_s = 0$), one can see that the magnitude of the shifts, proportional
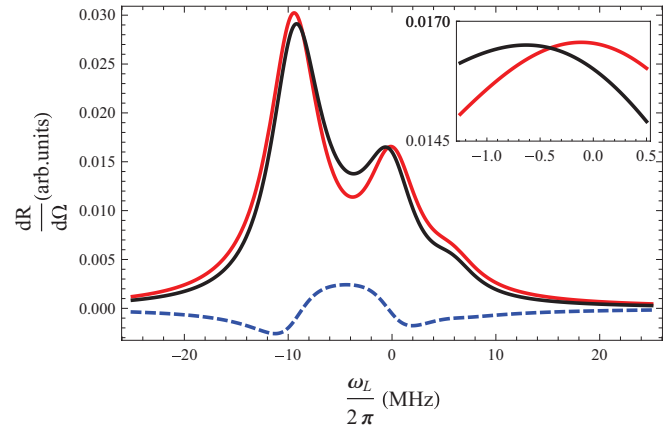

FIG. 2. (Color online) The scattering rate (or intensity), $\frac{dR}{d\Omega}$ in arbitrary units, of the $F = 2 \to F' = 1, 2, 3$ Doppler-free feature in ^{7}Li with $\theta_L = 0$. Red line shows the sum of Lorentzians with polarization independent weights, blue dashed line shows the sum of cross terms, black line shows the sum of Lorentzians and cross terms. The laser frequency $\omega_L/(2\pi)$ is the offset from the $F = 2 \to F' = 2$ peak in units of MHz. The inset is the $F = 2 \to F' = 2$ peak enlarged to show the shift in the line center.

to the angular-dependent terms, has maxima at $\theta_L = 0$, $\pi/2$ and the sign of the effect changes at $\theta_L = \theta_M$. This will be experimentally verified in the next section. The size of the shifts in Li are on the order of 100 kHz to 1 MHz; large enough to completely overshadow effects associated with Doppler shifts and optical pumping.

To provide an estimate for other transitions not explicitly considered here, we imagine atoms with the electronic structure of ^{6}Li or ^{7}Li with variable hyperfine coupling. We consider shifts of individual hyperfine components as the hyperfine splitting is varied. We intuitively expect that degenerate resonances would not affect the measured line position. In the opposite limit, $\Delta_{F'}^{F''}/\Gamma \gg 1$, we also expect the line positions to be unperturbed. These two limits imply that there must be an intermediate hyperfine splitting that maximally affects the measured line positions. We can see in Fig. 3 that this happens when $\Delta_{F'}^{F''}/\Gamma$ is of order one.

To get a feel for the apparent shifts of individual components as a function of separation, we consider a simple analytically solvable line shape consisting of two Lorentzian profiles with splitting Δ and equal amplitude. We take line profiles with and without cross terms and determine the component positions for each as the zero crossings of their first derivatives. We examine the difference of the position of the first component in the Lorentzian-only profile, x_L, and the position of the corresponding component in the full line profile including cross terms, x_F, as a function of the splitting Δ. In the limit of distantly spaced resonances, $\Delta/\Gamma \gg 1$, the difference in line centers is $x_F - x_L \simeq \Gamma^2/(4\Delta)$, in agreement with the large splitting limit described in Ref. [5]. These shifts at large separation have recently been calculated at the 1 kHz level in metastable He [21] and in principle occur in muonic hydrogen, although at ≈ 100 MHz they are much too small to account for the discrepancy between proton charge radius values [22,23]. In alkali metals with resolvable hyperfine structure, i.e., ^{87}Rb and ^{133}Cs, these shifts may also appear
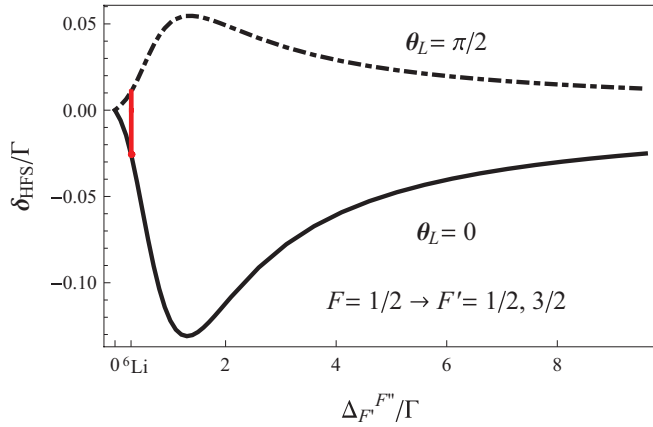
FIG. 3. (Color online) Error in the measured hyperfine splitting (in units of Γ) for a $F = 1/2 \rightarrow F' = 1/2, 3/2$ transition as a function of the assumed separation when the theoretically calculated full line shape is fit as the sum of two Lorentzians. The dash dotted (solid) curve is for laser polarization $\theta_L = \pi/2$ (0). The error in the hyperfine splitting is greatest where the assumed separation is about 1.3 times the natural line width. The red vertical line indicates the x position of the actual hyperfine splitting for ^{6}Li. Its vertical extent shows the range of errors that can occur when the laser polarization is varied between 0 and $\pi/2$.

at the ≈ 10 kHz level which, while much smaller than in unresolvable lines, is on the order of the reported experimental uncertainties [24,25]. This zero intensity shift may also arise from fine structure interference, and for Li is ≈ 860 Hz (below our experimental uncertainty). These shifts at large separation may be particularly insidious because they would only add a weak linear dependance to the background without deforming the line shape, as in the case of unresolvable features.

We also investigate the dependence of an unresolved feature's extracted center of gravity on hyperfine separation, as shown in Fig. 4. Using the same procedure, we generate the full line shape, now with three components ($F = 2 \rightarrow F' = 1, 2, 3$). We vary the splitting via the magnetic dipole constant, $A_{3/2}$, while fixing the electric quadrupole constant at the value appropriate for ^{7}Li. The same qualitative behavior occurs, producing extracted center-of-gravity shifts which are largest when $|A_{3/2}|$ ($\propto \Delta_{F'}^{F''}$) is of order Γ. There is now an additional feature; since there are two resonances that can shift relative to each other, the sign of the shift can change for a given laser polarization.

III. APPLICATION TO ^{6,7}LI EXPERIMENTAL DATA

Having discussed the nature and theoretical implications of quantum interference effects on the observed line shape, we apply our theoretical results to experimentally measured spectra of lithium taken at multiple laser polarization angles. Improved spectroscopy of the Li D lines (see Fig. 5 for level structure) is of broad interest in physics because the isotope shift of these lines may serve as a nuclear-model-independent method to measure relative nuclear charge radii, which are especially interesting in the neutron-rich ^{8,9,11}Li [26]. Measured isotope shifts for the lithium $2s$-$2p$ (D lines) [27–31] or $2s$-$3s$ [32–35] transitions can be combined with
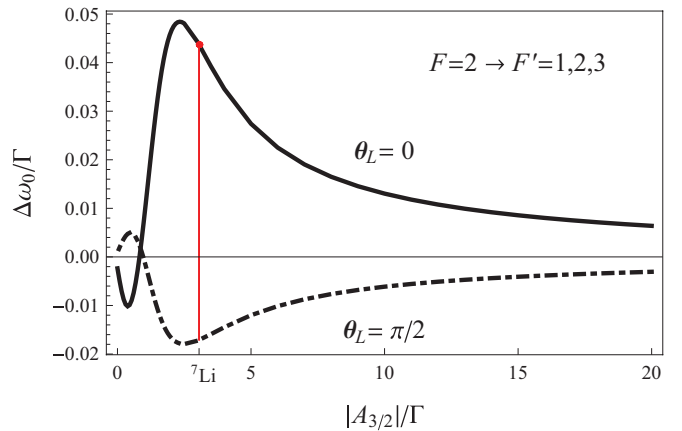

FIG. 4. (Color online) Error in the measured center of gravity (in units of Γ) for a $F = 2 \rightarrow F' = 1, 2, 3$ transition as a function of the hyperfine A constant when the theoretically calculated full line shape is fit as a sum of three Lorentzians. The dash dotted (solid) curve is for laser polarization $\theta_L = \pi/2$ (0). The red vertical line indicates the x position of the actual A constant for ^{7}Li. Its vertical extent shows the range of errors that can occur when the laser polarization is varied between 0 and $\pi/2$.

precise theoretical calculations [26,36,37] to determine the relative nuclear charge radii of lithium isotopes. Additionally, measured D-line transition frequencies are used as input for the calculation of species-specific "tune in or out" optical lattices for mixtures of quantum degenerate gases [38–40].

Our additional measurement and analysis provides a refined determination of the absolute transition frequencies of the ^{6,7}Li D_2 lines. When combined with previously measured D_1 values [6] these new data provide an improved measure of the ^{6,7}Li excited state fine structure, $2s$-$2p$ isotope shift, and the isotopic difference in the ^2P fine-structure splitting, the
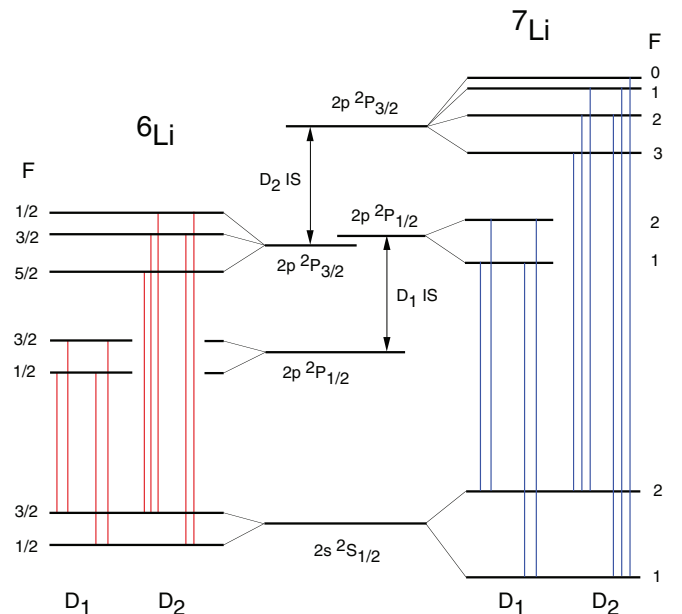

FIG. 5. (Color online) Relevant ^{6,7}Li level structure. The hyperfine components for the D_2 transition have natural widths of order of the hyperfine splitting. "IS" stands for isotope shift.
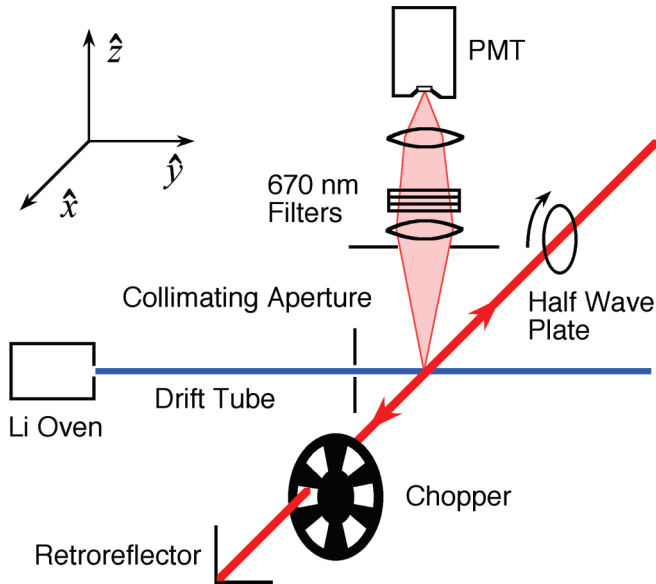
FIG. 6. (Color online) Simplified schematic of experimental apparatus. The interaction region is surrounded by three layers of mu-metal (not shown) to minimize the magnetic field. The coordinate system shown is consistent with Fig. 1.

splitting isotope shift (SIS). The SIS provides the best point of comparison between theory and experiment. We propose that the interference effect we describe here is the root cause for some disagreements between previous measurements in Li [27–30] and for the lack of internal consistency of the frequency-comb-based measurement in K [8].

A. Apparatus and procedure

A simplified schematic view of our apparatus [6,41] is shown in Fig. 6. Light from a single-frequency diode laser intersects a collimated thermal beam of lithium atoms at a right angle. A half wave plate controls the angle of polarization of the light. The laser beam is retroreflected by a precise corner cube that provides a return beam antiparallel to better than 1.45 μrad. The return beam is chopped at 500 Hz by a mechanical chopper. We observe the spectrum by scanning the laser frequency over a lithium component and record the fluorescence along an axis approximately orthogonal to both the laser and atomic beams. To minimize stray light, the interaction region is imaged on the photocathode through a stack of three narrow-band 670 nm interference filters.

The lithium beam is formed in a vacuum system with a background-gas pressure of less than 1.3×10^{-5} Pa (1×10^{-7} Torr). Lithium atoms effuse from an oven that is typically operated at 450 °C and are collimated to a beam with a divergence angle of 1.4 mrad by a 2 mm aperture at a distance of 1.4 m. Isotopically enriched ^{6}Li was added to the oven to produce a beam with approximately equal densities of the two naturally occurring isotopes.

The lithium resonances are probed by a diode laser at 670 nm that is locked to an evacuated Fabry-Perot cavity using the Pound-Drever-Hall method [42]. This servo-lock narrows and stabilizes the diode laser output. Despite the wide bandwidth of the servo, the laser line width is limited to about

500 kHz due to acoustic noise that couples to the cavity. The laser can be scanned under computer control by varying the voltage applied to a piezo electric stack to which one of the cavity mirrors is mounted. In the interaction region the laser is collimated to a 3.5-mm-diameter beam and the laser power was typically attenuated to 3 μW. Stability of the laser power over a single scan was better than 1%.

The lithium fluorescence signal is detected in two channels by a gated photon counter. One of these channels observes the fluorescence when both forward and return laser beams interact with the lithium beam. For the other channel the return beam is blocked by the chopper and the signal is attributable to the forward beam only. By differencing the photon count in the two channels, we recover the signal due to the reverse beam. In this way we obtain the forward and reverse signals simultaneously in a single scan with an optical setup in which the antiparallelism of the forward and reverse beams is limited only by the precision of the corner-cube retroreflector.

Our experiment differs from previous observations of the lithium D lines in that we measure directly the frequency of the laser using a femtosecond optical frequency comb [43]. The comb is a commercial instrument based on an Er fiber laser with a repetition rate of 250 MHz. The fiber laser output is frequency doubled and broadened with a photonic crystal fiber producing a comb with broad spectral coverage in the red and near-infrared regions. A low-resolution spectrometer is used to observe the spectral distribution of the comb to optimize the output at 670 nm. The repetition rate and carrier offset frequency of the comb are referenced to a stable quartz oscillator which is in turn locked to a cesium clock. This configuration produces a frequency reference with an absolute accuracy of better than 2 parts in 10^{13} and an Allan deviation of approximately 3×10^{-13} for integration times of 1 to 100 s. The frequency measurement using the comb is, therefore, a negligible contributor to our experimental uncertainty.

The spectroscopy laser is beat against a single tooth of the frequency comb using a high-speed photodetector and a narrow-band filter having a center frequency of 30 MHz and a width of about 6 MHz. To record a calibrated scan across a lithium line, the repetition rate of the frequency comb is first adjusted so that the beat frequency between an arbitrary mode of the comb and the spectroscopy laser is approximately 30 MHz. A computer-generated voltage ramp is then used to vary both the laser frequency and the comb repetition rate so that the beat frequency remains fixed at 30 MHz.

Data are recorded by scanning the laser across a lithium resonance in steps of approximately 250 kHz. A settling time of 200 ms is allowed after each step. Scans are acquired in pairs with increasing and decreasing laser frequency. Fluorescence data are accumulated alternately on the two gated-photon-counter channels for a total acquisition time of 72 ms on each channel. The beat-note frequency between the spectroscopy laser and the frequency comb is counted over the same time interval. For every data point, we record the comb repetition rate, comb offset frequency, beat-note frequency, beat-note signal strength, lithium fluorescence signal on both photon counter channels, and spectroscopy laser output power.

Doppler-free spectra of the Li D lines were taken at different laser polarization angles θ_L and fit using the line shapes presented here convolved with a Gaussian to account for

the residual Doppler broadening present in the experiment, typically ≈ 4 MHz. For resolved resonance features without a polarization dependence, such as the D_1 lines, the independent fitting parameters are the line center, the overall amplitude, a constant background offset, the natural width, and the Doppler width. The polarization angle of any given data set was fixed. For the unresolved fluorescence features, we limited the number of fitting parameters by fixing the excited-state hyperfine splittings to values calculated in Ref. [44] and in agreement with Ref. [45]. In addition we fixed the ratio of the unresolved amplitudes to values given by Eq. (9), with numerical values for $A_F^{F'}$, $B_F^{F'}$, and $C_F^{F',F''}$ tabulated in Appendix A. A small correction was made to account for the effect of the finite collection angle of the detector (see Appendix C).

B. Observation of apparent line-strength and transition frequency variation with θ_L

One of the most striking features present in the more complete line shapes is the change in the amount of scattered light with excitation polarization. A single fit to five spectra at different laser polarization angles demonstrates good overall agreement, including relative line strengths. Figure 7 shows the $F = 1/2 \rightarrow F' = 1/2, 3/2$ D_2 feature of ^{6}Li (center, $\omega_L/(2\pi) \approx 0$ MHz) and the $F = 2 \rightarrow F' = 1, 2$ D_1 peaks of ^{7}Li (left and right, $\omega_L/(2\pi) \approx \pm 50$ MHz). The ^{7}Li D_1 lines have no angular dependence (in general no D_1 lines have angular dependence). The presence of the D_1 lines enable the single fit to multiple data sets because they allow the effect of background light levels and laser intensity fluctuations to be compensated for in multiple spectra taken at different times. The fit to these five data sets used only one natural width and one (mass-scaled) Doppler width.
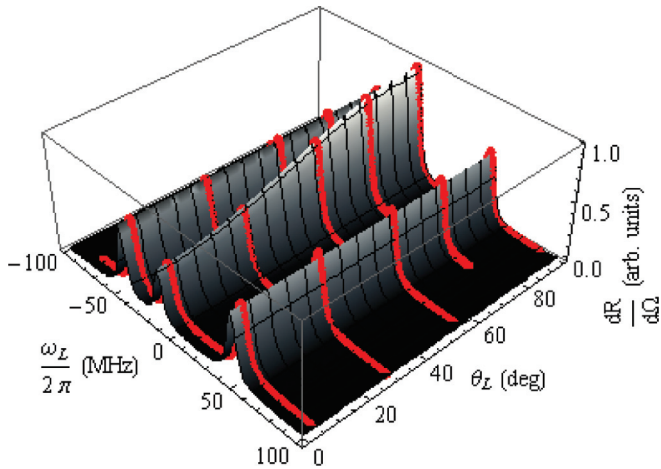

FIG. 7. (Color online) Amplitude of scattered light, proportional to Eq. (7), as a function of laser frequency ω_L and laser polarization angle θ_L. The laser frequency is offset from the ^{6}Li $F = 1/2$ ground state by 446 THz (see Table I for optical frequencies). The gray-scale surface is the complete theoretical line shape including cross terms and the red points are experimental data taken at $\theta_L = 0°, 25°, 51°, 75°$, and $90°$. The central feature is the $F = 1/2 \rightarrow F' = 1/2, 3/2$ transitions in ^{6}Li while the two constant amplitude side peaks are the $F = 1 \rightarrow F' = 1, 2$ D_1 lines of ^{7}Li.
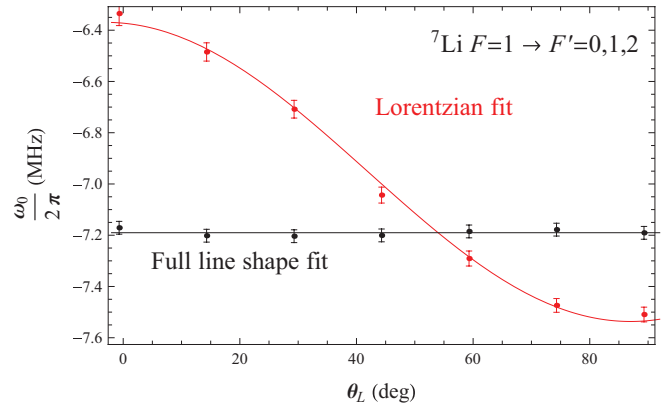

FIG. 8. (Color online) Line center of ^{7}Li $F = 1 \rightarrow F' = 0, 1, 2$ feature fit from experimentally measured spectra as a function of laser polarization angle with respect to the collection direction. Transition frequencies are offset from the ^{7}Li $F = 1$ ground state by 446 THz (see Table I for optical frequencies). The black (red) data points were extracted by fitting the data to functions with (without) interference cross terms. Error bars represent the uncertainties given in Table I.

To demonstrate the apparent transition frequency shifts resulting from analysis with an incomplete line shape in measured ^{7}Li D_2 data, we fit the same spectra taken at different laser polarizations and extract the line centers, with and without the cross terms. In Fig. 8, the red points are line centers fit without cross terms and the black points are the same data fit with the full theory. The black points are self consistent, independent of laser polarization while the red points exhibit a strong polarization dependence. The fit to the red data is of the form $A + B P_2(\cos \theta_L)$. The amplitude of the laser-polarization-dependent shift is of order 1 MHz.

Near the magic angle $\theta_L = \theta_M \approx 54.7°$ the Lorentzian fits give the same line center as the full line shape.

C. Discussion of systematics

1. Angular offset.

To accurately extract line positions at all polarizations, the angle θ_L between the laser polarization and the detection optics must be controlled and understood. Using a wave plate, we could precisely define θ_L up to a small unknown offset angle θ_0. We improved our previous estimate of θ_0 [6] by geometric measurements made when disassembling the apparatus, finding $\theta_0 = -0.7 (10)$ degrees.

As a consistency check, we compared the well-known ground-state hyperfine intervals (GHIs) to GHI values we measure by subtracting optical frequencies at multiple angles θ_L. We note that, for small offsets θ_0, the line shifts near $\theta_L = 0, \pi/2$ are insensitive to first order in θ_0 because the derivative of the angular dependence ($\propto \sin \theta_L \cos \theta_L|_{\theta_L=\gamma, \theta_s=0}$) vanishes. This is of practical utility since data fit at $\theta_L = 0, \pi/2$ with the complete line shape including cross terms should be accurate as well as equal to each other. We found that, while the GHIs derived from measurements of the resolved D_1 lines [6] were consistent with known values [46], the GHIs derived from the unresolved D_2 lines at $\theta_L = 0, \pi/2$ differed from the known values by as much as 30 kHz. This disagreement

indicates the importance of intensity-dependent shifts on the line shapes when cross terms are significant.

2. Intensity-dependent shifts.

For isolated lines, the fitted amplitudes are taken to be free parameters and the fitted line centers are independent of fitted amplitude. As a consequence, the centers of the resolved lines are not sensitive to intensity-dependent effects like optical pumping that modify the line ratios from their theoretical values. For unresolvable lines, however, the fitted line positions depend on the fixed relative values of f and g used in the fit. The unresolvable lines are therefore sensitive to intensity-dependent effects. To explore the impact of excitation-laser intensity on extracted line centers, we measured a subset of spectra at multiple laser powers and performed a full optical Bloch equation (OBE) simulation of the scattering, including all the ground and excited Zeeman levels [47,48]. We numerically solve the OBE with a time-dependent Rabi frequency proportional to the Gaussian intensity profile seen by the atom as it transverses the excitation-laser beam. We then generate a Doppler-free line shape by calculating the directional photon scattering rates derived from the OBE as a function of laser frequency. At the intensities used here and in Ref. [6], we find that these intensity-dependent effects are small but important (≈ 20 kHz). However, we suggest that larger previously reported uncertainties (≈ 100 kHz) in ^{39,41}K [8] ascribed to optical pumping could likely be removed by using a line shape that includes cross terms.

To quantitatively account for intensity-dependent light shifts and optical-pumping effects on the line positions, we generate numerical OBE data at several different intensities and fit the numerical data using the analytically calculated line strengths f and g appropriate for low intensity. (We confirm that in the low-intensity limit, the numerical data matches both the expected line positions and line strengths.) We then determine the linear intensity-dependent line shifts from this numerical data and apply this shift to the measured line positions [49]. The laser intensities were determined experimentally from the relative line strengths of the resolved features taken at different laser intensities. This estimate of the intensity is somewhat lower than estimates based on measured beam waists and laser power (typically 3.5 mm and 3 μW, respectively) but removes uncertainty associated with secondary measurements of beam waist and power. For most features, the shift was of order of a few kHz/μW, but for the ^{7}Li D_2 $F = 1 \rightarrow F' = 0, 1, 2$ transitions it was as large as 6.7 kHz/μW (for our beam waist). The uncertainty in this correction was set equal to the value of the applied shift and represents one of the largest sources of uncertainty in the experiment. For the unresolvable lines considered here, we find that optical pumping can have a larger systematic effect than the light shifts alone. Future experiments should be careful to work at low intensities to avoid these shifts on unresolvable lines.

3. Doppler correction.

The correction of the first-order Doppler effect was determined from simultaneously recorded forward and reverse beam signals using a corner cube to retroreflect the excitation laser beam. For the polarization-independent D_1 lines [6] the
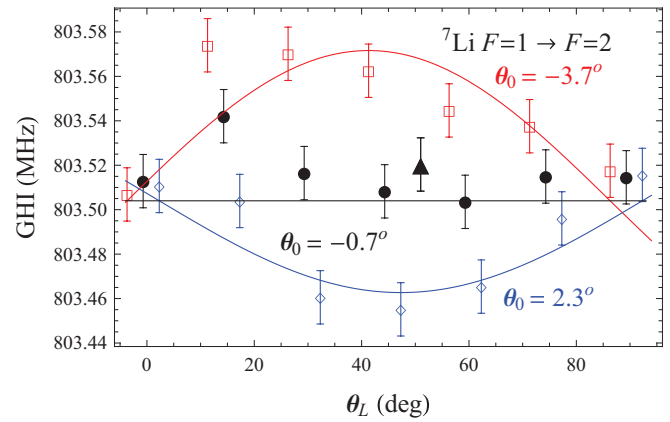

FIG. 9. (Color online) ^{7}Li ground-state hyperfine interval ($F = 1 \rightarrow F = 2$) as function of laser polarization angle. The measured GHI was determined by subtracting absolute measurements of the excited state $F = 1 \rightarrow F' = 0, 1, 2$ and $F = 2 \rightarrow F' = 1, 2, 3$ features including Doppler and intensity-dependent corrections (see the text). The red (black, blue) data are for an angular offset of $-3.7°$ ($-0.7°$, $2.3°$). The red (black, blue) curve is of the form $A_{\theta_0} \sin(\theta) \cos(\theta) + GHI_0$, where GHI_0 is the value measured in Ref. [46] and A_{θ_0} is fit to the data. The triangular point is data from Ref. [6] reanalyzed using the procedure described in the present work. Error bars represent the uncertainties given in Table I.

systematic contribution to the uncertainty of this correction is 1.4 kHz due to imperfections of the corner-cube retroreflector. Because the retroreflector does not preserve the laser polarization, the Doppler correction for the polarization-sensitive unresolved D_2 lines could not be determined using the corner cube and is taken instead from a linear fit of correction versus time for resolved components measured on the same day. This is necessary because the laser alignment drifts slightly over hours of data taking and results in a larger Doppler uncertainty of about 10 kHz.

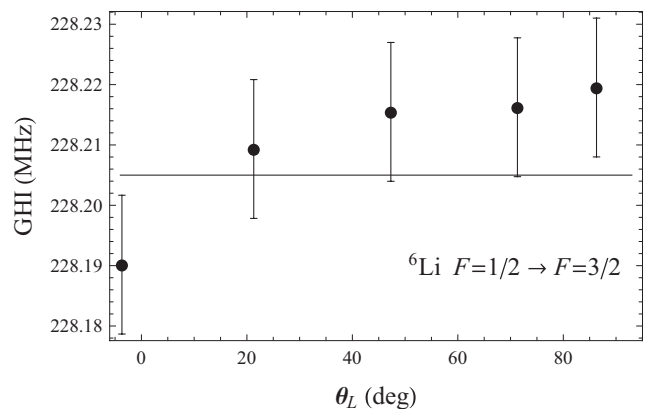FIG. 10. ^{6}Li ground-state hyperfine interval ($F = 1/2 \rightarrow F = 3/2$) as a function of laser polarization angle. The measured GHI was determined by subtracting absolute measurements of the excited state $F = 1/2 \rightarrow F' = 1/2, 3/2$ and $F = 3/2 \rightarrow F' = 1/2, 3/2, 5/2$ features. The solid line is the value measured in Ref. [46]. Error bars represent the uncertainties given in Table I.

TABLE I. Measured frequencies of hyperfine components and centers of gravity (cog) of the ^{6,7}Li D_2 lines.[a]

Line	F	F'	Frequency (MHz)
^{6}Li D_2	3/2	5/2	446799571.067 (21)
^{6}Li D_2	3/2	3/2	446799573.962 (21)
^{6}Li D_2	3/2	1/2	446799575.673 (21)
^{6}Li D_2	1/2	3/2	446799802.172 (16)
^{6}Li D_2	1/2	1/2	446799803.883 (16)
^{6}Li D_2 cog			446799648.870 (15)
^{7}Li D_2	2	3	446809874.895 (20)
^{7}Li D_2	2	2	446809884.357 (20)
^{7}Li D_2	2	1	446809890.170 (20)
^{7}Li D_2	1	2	446810687.873 (25)
^{7}Li D_2	1	1	446810693.687 (25)
^{7}Li D_2	1	0	446810696.445 (25)
^{7}Li D_2 cog			446810183.163 (16)

[a]Unresolved component splittings for the D_2 lines are fixed at values calculated from the hyperfine A and B constants of Ref. [44].

D. Results: Absolute transition frequencies, excited-state hyperfine splitting, isotope shift, and splitting isotope shift

Including the Doppler corrections and the power-dependent shifts, the GHI values at $\theta_L = 0, \pi/2$ are in agreement with each other and the known values [46] (see Figs. 9 and 10). The value of θ_0 that minimizes the $\sin\theta_L \cos\theta_L$ angular dependence is consistent with the geometrically determined value. The final reported line positions, shown in Table I, represent an average over θ_L. A representative uncertainty budget is given in Table II.

Measurements at multiple laser polarizations analyzed with the correct line shape provide an important tool to independently estimate systematic errors associated with the offset angle θ_0. For example, power-dependent shifts such as optical pumping can partially cancel the effect of θ_0 on the line shape and GHI. Minimizing residuals and comparing the GHI near θ_m can still lead to small systematic shifts in the line positions. These effects are more prominent in ^{7}Li than ^{6}Li, and our new determinations of the centers-of-gravity of the absolute transition frequencies differ from our previous results [6], by 83 and 19 kHz, respectively. From the absolute frequencies the excited-state fine-structure splitting (Table III), as well

TABLE II. Representative uncertainty budget (kHz).

Uncertainty component	^{6}Li D_2 $F = 3/2 \to F' = 5/2, 3/2, 1/2$
Statistical variation	4
First-order Doppler effect	10
Estimate of θ_m	3
Laser-power-dependent shifts[a]	17
Laser-intensity variation	3
Hyperfine constant inaccuracy	2
Imaging system imperfections	2
Magnetic-field shift	<1
Reference frequency	0.089
Total	21

[a]Optical pumping, multiple excitation recoil, ac Stark shift.

TABLE III. Excited-state fine-structure intervals.

Interval[a]	Splitting (MHz)	Ref.
^{6}Li $2p$ ^2P fs	10052.779 (17)	This work
^{6}Li $2p$ ^2P fs	10052.799 (22)	Sansonetti [6]
^{6}Li $2p$ ^2P fs	10052.76 (22)	Brog [50]
^{6}Li $2p$ ^2P fs	10052.044 (91)	Walls [29]
^{6}Li $2p$ ^2P fs	10052.964 (50)	Noble [30]
^{6}Li $2p$ ^2P fs	10052.862 (41)	Das [31]
^{6}Li $2p$ ^2P fs	10050.932 (8)[b]	Puchalski (theory) [44]
^{7}Li $2p$ ^2P fs	10053.310 (17)	This work
^{7}Li $2p$ ^2P fs	10053.393 (21)	Sansonetti [6]
^{7}Li $2p$ ^2P fs	10053.184 (58)	Orth [51]
^{7}Li $2p$ ^2P fs	10052.37 (11)	Walls [29]
^{7}Li $2p$ ^2P fs	10053.119 (58)	Noble [30]
^{7}Li $2p$ ^2P fs	10051.999 (41)	Das [31]
^{7}Li $2p$ ^2P fs	10051.477 (8)[b]	Puchalski (theory) [44]

[a]All D_1 values are taken on the same apparatus and reported in Ref. [6].

[b]The uncertainties reported in [44] represent only the numerical uncertainty and do not include any estimate of the size of corrections not included in the calculations.

as the $2s$-$2p$ IS and the SIS (Table IV) are calculated and compared to the existing literature. As discussed in Ref. [37], both quantum electrodynamic and nuclear-size corrections largely cancel when calculating the SIS. It is, therefore, the most reliable result of theory and has been suggested as a benchmark for testing the internal consistency of experimental data. Previously reported results have disagreed with each other and with theory far beyond their reported uncertainties (Table IV). Our current result resolves these discrepancies and is in full agreement with the most recent theoretical result [44]. This supports the theory that underlies the use of D-line ISs to determine mean-square nuclear charge radii for short-lived Li isotopes.

IV. EXTRACTION OF RELATIVE NUCLEAR CHARGE RADII

Finally, we calculate the difference in the ^{6,7}Li nuclear charge radii using the measured D_2 isotope shifts reported in

TABLE IV. ^{7,6}Li isotope shifts.

Transition	Shift (MHz)	Ref.
D_2 IS	10534.293 (22)	This work
D_2 IS	10534.357 (29)	Sansonetti [6]
D_2 IS	10533.59 (14)	Walls [29]
D_2 IS	10534.194 (104)	Noble [30]
D_2 IS	10533.352 (68)	Das [31]
SIS[a]	0.531 (24)	This work
SIS	0.594 (30)	Sansonetti [6]
SIS	-0.67 (14)	Walls [29]
SIS	0.155 (60)	Noble [30]
SIS	-0.863 (79)	Das [31]
SIS	0.396 (9)	Yan (theory) [37]
SIS	0.5447 (1)	Puchalski (theory) [44]

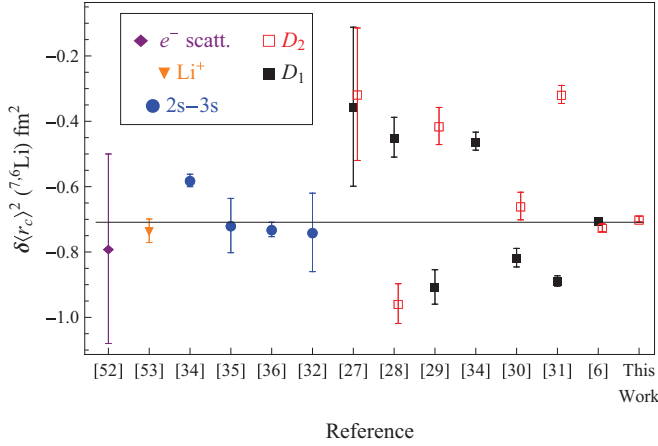[a]All D_1 values are taken on the same apparatus and reported in Ref. [6].

FIG. 11. (Color online) Measurements of difference in mean-square charge radius between ^{7}Li and ^{6}Li. The points are grouped by type of measurement and are then ordered chronologically within different types of measurement. The solid black line is the weighted average of the results of Refs. [36,52,53], along with the D_1 value from [6] and the D_2 value from this work. Error bars for the present work represent the uncertainties given in Table IV; all other error bars represent the uncertainties given in the original references.

Table IV and the D_1 shifts reported in Ref. [6]. This serves as a point of comparison amongst different types of measurements including elastic electron scattering [52], optical isotope shift measurements on the $^3S_1 \rightarrow {}^3P_{0,1,2}$ transition in Li$^+$ [53], and optical isotope shift measurements of the $2s$-$3s$, D_1, and D_2 transitions in neutral Li [27–35] as shown in Fig. 11. We calculate the difference in nuclear charge radius using Eq. (40) of Ref. [26],

$$\delta\langle r_c^2\rangle(^{7,6}\mathrm{Li}) = \langle r_c^2\rangle(^7\mathrm{Li}) - \langle r_c^2\rangle(^6\mathrm{Li}) = \frac{(E_{\mathrm{meas}} - E_0)}{C_0}, \quad (10)$$

where $\langle r_c^2\rangle(^i\mathrm{Li})$ is the mean-square nuclear charge radius of the ith isotope in fm^2, E_{meas} is the measured isotope shift in MHz, $E_0 = -10\,532.5682$ ($-10\,532.0237$) MHz is the theoretically calculated isotope shift excluding the finite size corrections for the $D_2(D_1)$ transitions [54], and $C_0 = -2.4658$ MHz/fm^2 [54].

The values of the difference in mean-square nuclear charge radius are $-0.705\,(3)$ fm^2 for the D_1 and $-0.700\,(9)$ fm^2 for the D_2 lines. These values are self-consistent and have the smallest uncertainties among those shown in Fig. 11. They bring the D-line measurements into full agreement with the best values from electron scattering and optical IS measurements on $2s$-$3s$ and $^3S_1 \rightarrow {}^3P_{0,1,2}$ transitions in Li and Li$^+$, respectively.

V. CONCLUSION

We reviewed low-intensity scattering theory as it applies to the spectroscopy of alkali-metal atoms with unresolvable hyperfine structures. We find that the effects of light polarization and quantum interference alter the relative line strengths and quantitatively affect the extraction of transition frequencies from data, even in the low-intensity limit. Optical pumping effects at finite excitation power can further complicate the

line shape, which we account for numerically. This leads to a revised determination of the ^{6,7}Li D_2 line frequencies and splitting isotope shift. We identify several species: H [7], ^{22,23}Na [55], ^{39,40,41}K [8], and $^{220-228}$Fr [9], ^{7,9,11}Be II [10], and ^{25}Mg II [11], for which these complete line shapes will enable the next generation of measurements.

APPENDIX A

1. Expressions for the normalized dipole matrix elements.

The vector components of **A** are easiest to describe in the spherical vector basis A_q appropriate for σ^+, π, and σ^- light, where

$$A_1 = -(A_x + iA_y)/\sqrt{2}, \quad A_0 = A_z,$$
$$A_{-1} = (A_x - iA_y)/\sqrt{2}. \quad (A1)$$

Using the Wigner-Eckart theorem, the dipole matrix elements are given in terms of reduced matrix elements as

$$\left(D_{Fm}^{F'm'}\right)_q = \frac{\langle F'||\mathbf{D}||F\rangle}{\sqrt{2F'+1}}\langle Fm; 1q|F'm'\rangle, \quad (A2)$$

where $\langle Fm; 1q|F'm'\rangle$ is the Clebsch-Gordan coefficient for adding $|F,m\rangle$ to $|1,q\rangle$ to get $|F',m'\rangle$. Under the assumption that the hyperfine interaction does not modify the electronic structure of the state, the F-reduced matrix elements can be written in terms of J-reduced elements

$$\langle F'||\mathbf{D}||F\rangle = \langle J'||\mathbf{D}||J\rangle\sqrt{f_F^{F'}}, \quad (A3)$$

where the reduced oscillator strength $f_F^{F'}$ for the F-F' transition can be written in terms of Wigner 6-j symbols:

$$\sqrt{f_F^{F'}} = (-1)^{F+I+1+J'}\sqrt{2F+1}\sqrt{2F'+1}\begin{Bmatrix} J' & J & 1 \\ F & F' & I \end{Bmatrix}. \quad (A4)$$

Defining the components of the matrix elements $(\mathbf{A}_{Fm}^{F'm'})_q$ for each $J \rightarrow J'$ transition

$$\left(\mathbf{A}_{Fm}^{F'm'}\right)_q = \frac{\sqrt{2J'+1}}{\sqrt{2F'+1}}\langle Fm; 1q|F'm'\rangle\sqrt{f_F^{F'}}, \quad (A5)$$

the dipole matrix elements can be written as

$$\left(D_{Fm}^{F'm'}\right)_q = \frac{\langle J'||\mathbf{D}||J\rangle}{\sqrt{2J'+1}}\left(\mathbf{A}_{Fm}^{F'm'}\right)_q. \quad (A6)$$

Pulling the reduced matrix element $\langle J'||\mathbf{D}||J\rangle$ out of the sum, Eq. (2) can be written in terms of the inverse scattering rate Γ and a saturation intensity I_0:

$$\Gamma = \frac{1}{\tau} = \frac{\omega^3}{3\pi\epsilon_0\hbar c^3}\frac{|\langle J'||\mathbf{D}||J\rangle|^2}{(2J'+1)}, \quad (A7)$$

TABLE V. D_2 weights and cross terms for $I = 1/2$ applicable to H, ^{11}Be II.

F	F'	F''	$A_F^{F'}$	$B_F^{F'}$	$C_F^{F',F''}$
0	1		1/18	−1/36	
1	1	2	1/12	1/48	−1/16
1	2		5/12	−7/48	

and

$$I_0 = \frac{\pi h c \Gamma}{3\lambda^3}, \qquad (A8)$$

giving Eq. (3), where ω and λ are the frequency and wavelength of the transition, respectively.

APPENDIX B

1. Calculation of weights f and g.

The dipole radiation weights f and g are calculated using the expression for $\mathbf{A}_{Fm}^{F'm'}$ [Eq. (A5)] to determine $C_{i \to f}^{F'}$ [Eq. (4)], evaluating the sums in Eq. (7) and then comparing with the dipole radiation pattern (9). Taking k_s along $\hat{z}$, (i.e., $\theta_s = 0$), with the two scattered polarizations $\hat{\epsilon}_{s1} = \hat{x}$ and $\hat{\epsilon}_{s2} = \hat{y}$, and $\hat{\epsilon}_L$ to lie in the $\hat{z}$-$\hat{y}$ plane as in Fig. 1, the terms in the sum are given by

$$\hat{\epsilon}_{s1} \cdot \mathbf{A}_{Fm}^{F'm'} = \frac{-1}{\sqrt{2}} \left[\left(\mathbf{A}_{Fm}^{F'm'} \right)_1 - \left(\mathbf{A}_{Fm}^{F'm'} \right)_{-1} \right], \qquad (B1)$$

$$\hat{\epsilon}_{s2} \cdot \mathbf{A}_{Fm}^{F'm'} = \frac{i}{\sqrt{2}} \left[\left(\mathbf{A}_{Fm}^{F'm'} \right)_1 + \left(\mathbf{A}_{Fm}^{F'm'} \right)_{-1} \right], \qquad (B2)$$

$$\hat{\epsilon}_L \cdot \mathbf{A}_{Fm}^{F'm'} = \frac{i \sin \theta_L}{\sqrt{2}} \left[\left(\mathbf{A}_{Fm}^{F'm'} \right)_1 + \left(\mathbf{A}_{Fm}^{F'm'} \right)_{-1} \right]$$
$$+ \cos \theta_L \left(\mathbf{A}_{Fm}^{F'm'} \right)_0. \qquad (B3)$$

We report line weights and cross terms for the D_2 transitions, $^2S_{1/2} \to {}^2P_{3/2}$, of alkali-metal atoms and hydrogen with $I = 1/2$, 1, and 3/2 in Tables V, VI, and VII, respectively.

Note that there is no angular dependence to the D_1 terms and therefore no dipole dependence ($B_F^{F'} = C_F^{F',F''} = 0$ for D_1). Also note that $C_F^{F',F''} = C_F^{F'',F'}$. Physically, this is because scattering through F'' is indistinguishable from scattering through F' when the F'' and F' are overlapped within the natural width.

TABLE VI. D_2 weights and cross terms for $I = 1$ applicable to ^{2}H and ^{6}Li, ^{28}Na.

F	F'	F''	$A_F^{F'}$	$B_F^{F'}$	$C_F^{F',F''}$
1/2	1/2	3/2	8/18	0	−4/81
1/2	3/2		10/81	−1/81	
3/2	1/2	3/2	1/81	0	2/405
3/2	3/2	5/2	8/81	16/2025	−14/225
3/2	5/2	1/2	1/3	−7/75	−1/90

TABLE VII. D_2 weights and cross terms for $I = 3/2$ applicable to ^{7,9,11}Li, ^{21,23,34}Na, ^{39,41}K, and ^{87}Rb, ^{7,9}Be II.

F	F'	F''	$A_F^{F'}$	$B_F^{F'}$	$C_F^{F',F''}$
1	0	1	1/24	0	0
1	1	2	5/48	−1/48	−1/32
1	2	0	5/48	0	−1/48
2	1	2	1/48	1/1200	1/160
2	2	3	5/48	0	−7/120
2	3	1	7/24	−7/100	−7/400

APPENDIX C

1. Collection optics correction.

If fluorescence is collected over all solid angle there is no polarization-dependent modification to the line shape. The equations given in the text are valid for light scattered into an infinitesimal solid angle. Here we find the modification to the angular-dependent part of the line weights and cross terms due to the finite numerical aperture of the fluorescence collection optics. For a given laser polarization $\hat{\epsilon}_L$, we may integrate over the final scattering directions $\hat{k}_s$ allowed by the collection optics (parameterized by θ_s, ϕ_s):

$$\hat{\epsilon}_L = \sin \theta_L \, \hat{y} + \cos \theta_L \, \hat{z},$$
$$\hat{k}_s = \sin \theta_s \cos \phi_s \, \hat{x} + \sin \theta_s \sin \phi_s \, \hat{y} + \cos \theta_s \, \hat{z}, \quad (C1)$$
$$\hat{\epsilon}_L \cdot \hat{k}_s = \cos \gamma,$$

Performing the angular integrations over the isotropic part, where $d\Omega_s = d\phi d \cos(\theta_s)$, we find

$$\iint_{0,0}^{2\pi, \theta_C} d\Omega_s = 2\pi (1 - \cos \theta_C) \equiv S_0. \qquad (C2)$$

The angle-dependent dipole part is scaled by

$$\iint_{0,0}^{2\pi, \theta_C} d\Omega_s P_2(\cos \gamma) = \pi \cos \theta_C \sin^2 \theta_C P_2(\cos \theta_L)$$
$$\equiv S_2 P_2(\cos \theta_L). \qquad (C3)$$

Here θ_C is the half angle of the fluorescence collection cone. For determining experimentally relevant fitting functions, the ratio of the constant and dipole part is important, and we find that the dipole components are reduced relative to the constant components as

$$S_2/S_0 = \cos \theta_C \cos^2 \left(\frac{\theta_C}{2} \right). \qquad (C4)$$

These scaling factors are included as part of the fitting functions to account for the numerical aperture of the imaging system. Failure to include these scaling factors shifts the extracted line centers by ≈ 6 kHz for $\theta_C = 26.6º$ used in this experiment.

[1] V. Weisskopf and E. Wigner, Z. Phys. A: Hadrons Nucl. **63**, 54 (1930).

[2] P. A. Franken, Phys. Rev. **121**, 508 (1961).

[3] T. Bergeman, J. Chem. Phys. **61**, 4515 (1974).

[4] R. Walkup, A. L. Migdall, and D. E. Pritchard, Phys. Rev. A **25**, 3114 (1982).

[5] M. Horbatsch and E. A. Hessels, Phys. Rev. A **82**, 052519 (2010).

[6] C. J. Sansonetti, C. E. Simien, J. D. Gillaspy, J. N. Tan, S. M. Brewer, R. C. Brown, S. Wu, and J. V. Porto, Phys. Rev. Lett. **107**, 023001 (2011); **109**, 259901(E) (2012).

[7] K. S. E. Eikema, J. Walz, and T. W. Hänsch, Phys. Rev. Lett. **86**, 5679 (2001).

[8] S. Falke, E. Tiemann, C. Lisdat, H. Schnatz, and G. Grosche, Phys. Rev. A **74**, 032503 (2006).

[9] A. Coc, C. Thibault, F. Touchard, H. Duong, P. Juncar, S. Liberman, J. Pinard, J. Lerm, J. Vialle, S. Bttgenbach, A. Mueller, and A. Pesnelle, Phys. Lett. B **163**, 66 (1985).

[10] M. Žáková, Z. Andjelkovic, M. L. Bissell, K. Blaum, G. W. F. Drake, C. Geppert, M. Kowalska, J. Krämer, A. Krieger, M. Lochmann, T. Neff, R. Neugart, W. Nörtershäuser, R. Sánchez, F. Schmidt-Kaler, D. Tiedemann, Z.-C. Yan, D. T. Yordanov, and C. Zimmermann, J. Phys. G **37**, 055107 (2010).

[11] C. Sur, B. K. Sahoo, R. K. Chaudhuri, B. P. Das, and D. Mukherjee, Eur. Phys. J. D **32**, 25 (2005).

[12] R. Loudon, *The Quantum Theory of Light*, 3rd ed. (Oxford University Press, New York, 2000).

[13] P. A. M. Dirac, Proc. R. Soc. London, Ser. A **114**, 243 (1927).

[14] One may consider whether the interference effects described in this paper could also modify the simple replacement $\omega_{ji} \rightarrow \omega_{ji} + i\Gamma_j/2$ when accounting for the coupling to the continuum. However, in the cases considered here (a single electronic state split by fine and hyperfine structure), the effect of interference disappears when integrated over all solid angle. Since the inclusion of Γ_j results from summing the coupling to the continuum over all solid angle, it is probable that the addition of $i\Gamma_j/2$ correctly accounts for the continuum, although a more detailed calculation would be needed to confirm this. Empirically, the line shapes presented here fit well the observed data.

[15] J. F. Kielkopf, J. Opt. Soc. Am. **63**, 987 (1973).

[16] A. Corney, *Atomic and Laser Spectroscopy* (Oxford, New York, 1977).

[17] Alternatively, $\hat{\epsilon}_L$ could be fixed along $\hat{z}$, and $\mathbf{k}_s$ could be characterized by polar angles (θ'_s, ϕ'_s). This would have the advantage that $\theta'_s = \gamma$, but it is more convenient for a fixed scattering geometry to have θ_L be one of the free parameters.

[18] G. B. Arfken and H.-J. Weber, *Mathematical Methods For Physicists*, 6th ed. (Elsevier, New York, 2005).

[19] J. S. Deech, R. Luypaert, and G. W. Series, J. Phys. B: At. Mol. Phys. **8**, 1406 (1975).

[20] W. Demtroder, *Laser Spectroscopy: Basic Concepts and Instrumentation*, 3rd ed. (Springer-Verlag, Berlin, New York, 2003), p. 692.

[21] A. Marsman, M. Horbatsch, and E. A. Hessels, Phys. Rev. A **86**, 040501 (2012).

[22] R. Pohl *et al.*, Nature (London) **466**, 213 (2010).

[23] P. J. Mohr, B. N. Taylor, and D. B. Newell, Rev. Mod. Phys. **80**, 633 (2008).

[24] J. Ye, S. Swartz, P. Jungner, and J. L. Hall, Opt. Lett. **21**, 1280 (1996).

[25] V. Gerginov, C. E. Tanner, S. Diddams, A. Bartels, and L. Hollberg, Phys. Rev. A **70**, 042505 (2004).

[26] Z.-C. Yan and G. W. F. Drake, Phys. Rev. A **61**, 022504 (2000).

[27] C. J. Sansonetti, B. Richou, R. Engleman, and L. J. Radziemski, Phys. Rev. A **52**, 2682 (1995).

[28] W. Scherf, O. Khait, H. Jger, and L. Windholz, Z. Phys. D: At., Mol. Clusters **36**, 31 (1996).

[29] J. Walls, R. Ashby, J. Clarke, B. Lu, and W. van Wijngaarden, Eur. Phys. J. D **22**, 159 (2003).

[30] G. A. Noble, B. E. Schultz, H. Ming, and W. A. van Wijngaarden, Phys. Rev. A **74**, 012502 (2006).

[31] D. Das and V. Natarajan, Phys. Rev. A **75**, 052508 (2007).

[32] Y.-H. Lien, K.-J. Lo, H.-C. Chen, J.-R. Chen, J.-Y. Tian, J.-T. Shy, and Y.-W. Liu, Phys. Rev. A **84**, 042511 (2011).

[33] R. Sánchez, M. Žáková, Z. Andjelkovic, B. A. Bushaw, K. Dasgupta, G. Ewald, C. Geppert, H.-J. Kluge, J. Krämer, M. Nothhelfer, D. Tiedemann, D. F. A. Winters, and W. Nörtershäuser, New J. Phys. **11**, 073016 (2009).

[34] B. A. Bushaw, W. Nörtershäuser, G. Ewald, A. Dax, and G. W. F. Drake, Phys. Rev. Lett. **91**, 043004 (2003).

[35] G. Ewald, W. Nörtershäuser, A. Dax, S. Götte, R. Kirchner, H.-J. Kluge, T. Kühl, R. Sanchez, A. Wojtaszek, B. A. Bushaw, G. W. F. Drake, Z.-C. Yan, and C. Zimmermann, Phys. Rev. Lett. **93**, 113002 (2004).

[36] W. Nörtershäuser, R. Sánchez, G. Ewald, A. Dax, J. Behr, P. Bricault, B. A. Bushaw, J. Dilling, M. Dombsky, G. W. F. Drake, S. Götte, H.-J. Kluge, T. Kühl, J. Lassen, C. D. P. Levy, K. Pachucki, M. Pearson, M. Puchalski, A. Wojtaszek, Z.-C. Yan, and C. Zimmermann, Phys. Rev. A **83**, 012516 (2011).

[37] Z.-C. Yan, W. Nörtershäuser, and G. W. F. Drake, Phys. Rev. Lett. **100**, 243002 (2008).

[38] L. J. LeBlanc and J. H. Thywissen, Phys. Rev. A **75**, 053612 (2007).

[39] B. Arora, M. S. Safronova, and C. W. Clark, Phys. Rev. A **84**, 043401 (2011).

[40] M. S. Safronova, U. I. Safronova, and C. W. Clark, Phys. Rev. A **86**, 042505 (2012).

[41] C. E. Simien, S. M. Brewer, J. N. Tan, J. D. Gillaspy, and C. J. Sansonetti, Can. J. Phys. **89**, 59 (2011).

[42] R. Drever, J. Hall, F. Kowalski, J. Hough, G. Ford, A. Munley, and H. Ward, Appl. Phys. B: Photophys. Laser Chem. **31**, 97 (1983).

[43] T. Udem, R. Holzwarth, and T. W. Hänsch, Nature (London) **416**, 233 (2002).

[44] M. Puchalski and K. Pachucki, Phys. Rev. A **79**, 032510 (2009).

[45] V. A. Yerokhin, Phys. Rev. A **78**, 012513 (2008).

[46] A. Beckmann, K. D. Böklen, and D. Elke, Z. Phys. A: Hadrons Nucl. **270**, 173 (1974).

[47] C. Cohen-Tannoudji, J. Dupont-Roc, and G. Grynberg, *Optical Bloch Equations* in Atom-Photon Interactions (Wiley-VCH Verlag GmbH, New York, 2008), pp. 353–405.

[48] S. M. Tan, J. Opt. B: Quantum Semiclassical Opt. **1**, 424 (1999).

[49] Another approach might be to fit the numerical data with free line weights and use the determined intensity-dependent line weight ratios in the experimental fits. This provides a large number of free parameters, however, and the fits to numerical data were unstable in some cases.

[50] K. C. Brog, T. G. Eck, and H. Wieder, Phys. Rev. **153**, 91 (1967).

[51] H. Orth, H. Ackermann, and E. W. Otten, Z. Phys. A: At. Nucl. **273**, 221 (1975).

[52] C. D. Jager, H. D. Vries, and C. D. Vries, At. Data Nucl. Data Tables **14**, 479 (1974).

[53] E. Riis, A. G. Sinclair, O. Poulsen, G. W. F. Drake, W. R. C. Rowley, and A. P. Levick, Phys. Rev. A **49**, 207 (1994).

[54] M. Puchalski, D. Kedziera, and K. Pachucki, preceeding paper, Phys. Rev. A **87**, 032503 (2013).

[55] Y. Gangrsky, D. Karaivanov, K. Marinova, B. Markov, L. Melnikova, G. Mishinsky, S. Zemlyanoi, and V. Zhemenik, Eur. Phys. J. A **3**, 313 (1998).